Bin Xu
Department of Automotive Engineering,
Clemson University,
Greenville, SC 29607
e-mail: xbin@clemson.edu

Adamu Yebi
Department of Automotive Engineering,
Clemson University,
Greenville, SC 29607
e-mail: ayebi@g.clemson.edu

Dhruvang Rathod[1]
Department of Automotive Engineering,
International Center for Automotive Research,
Clemson University,
Greenville, SC 29607
e-mail: dhruvar@clemson.edu

Simona Onori
Department of Energy Resources,
Stanford University,
Stanford, CA 94305
e-mail: sonori@stanford.edu

Zoran Filipi
Department of Automotive Engineering,
Clemson University,
Greenville, SC 29607
e-mail: zfilipi@clemson.edu

Mark Hoffman
College of Engineering,
Mechanical Engineering,
Auburn University,
Auburn, AL 36849
e-mail: mah0142@auburn.edu

Experimental Validation of Nonlinear Model Predictive Control for a Heavy-Duty Diesel Engine Waste Heat Recovery System

This paper discusses an experimental validation of a real-time augmented control scheme for an organic Rankine cycle (ORC) waste heat recovery (WHR) system. A nonlinear model predictive control (NMPC) is designed to regulate the working fluid vapor temperature after the evaporator. The NMPC utilizes a six-state reduced order moving boundary (MB) evaporator model. The state estimator is constructed using an extended Kalman filter (EKF) given the working fluid outlet vapor temperature and exhaust gas outlet temperature as measurements. Working fluid evaporation pressure is controlled by an external proportional-integral-derivative (PID) control loop. The experimental validation first compares the performance of the augmented control scheme with that of a traditional multiple loop PID control with a feedforward term over an engine transient. The experimental study shows that the augmented control scheme outperforms the baseline multi-loop PID control in both terms tracking error and settling time during transient engine operation. The performance of the augmented control scheme is further validated over three additional transient conditions with alterations to both the engine transient and the working fluid reference temperature. The NMPC validation shows that the working fluid vapor temperature can be controlled within 1% error margin relative to the targeted reference. [DOI: 10.1115/1.4046152]

Keywords: model predictive control, heavy-duty diesel engine, organic Rankine cycle, waste heat recovery, extended Kalman filter

1 Introduction

Less than 50% of the fuel energy consumed by a heavy-duty diesel (HDD) engine creates useful work, with the remaining energy wasted as heat. Considering the large amount of wasted heat and the substantial size of the worldwide HDD fleet, HDD engine waste heat recovery (WHR) technologies have been well researched in the past decade. Through the inclusion of WHR techniques, HDD fuel economy can be improved by 2–6% [1–3].

Among the existing technologies, organic Rankine cycle (ORC) systems are considered a viable and mature technology for their relative cost effectiveness and high WHR efficiency. The ORC system uses waste heat sources (e.g., engine tail pipe (TP) exhaust gas) to vaporize a working fluid via heat exchangers [4]. The working fluid experiences phase change from liquid to vapor in an evaporator and then passes through the expander to produce power. After expansion, a condenser extracts the remaining heat from working fluid vapor, condensing it back to liquid phase.

In the past decade, the published studies made noticeable progress in the HDD engine ORC-WHR field. Teng et al. conducted a series of ORC-WHR studies on a heavy-duty engine, which included thermodynamic cycle analysis [5], working fluid selection [6], ORC system development [7], and experimental implementation [1]. These studies concluded that ethanol has potential as an ORC working fluid and that a 3–5% fuel economy improvement can be achieved using both the TP and exhaust gas recirculation gases as heat sources. Nelson gave several presentations on HDD engine ORC-WHR design, which included system sizing [8], engine efficiency contribution split by technologies [9], and preliminary experimental results [10]. Overall, the ORC-WHR system development methodology can be divided into several stages, as shown in Fig. 1. Note that control development connects the system integration, power optimization, and experimental implementation portions of the process. Without formal control development, experiments must be manually operated at steady engine speed and torque, making it impossible to collect valuable data during transient engine conditions. In addition, after the system development stage, a controller is crucial for efficient ORC system operation in production vehicles. Therefore, control development is a key step in the ORC-WHR system development process.

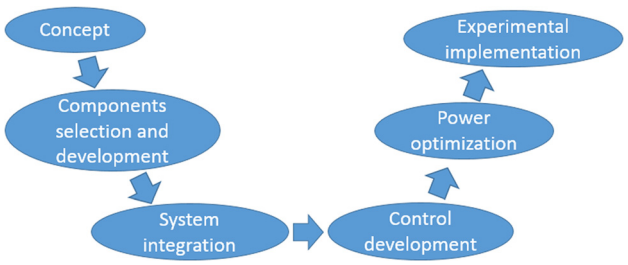

Fig. 1 ORC-WHR system development procedures

[1]Corresponding author.

Contributed by the Dynamic Systems Division of ASME for publication in the Journal of Dynamic Systems, Measurement, and Control. Manuscript received August 21, 2018; final manuscript received January 8, 2020; published online February 14, 2020. Assoc. Editor: Carrie Hall.

Organic Rankine cycle-WHR system control development is a challenging task. Thermal inertia of the aftertreatment system (i.e., the selective catalytic reduction and diesel particulate filter devices) delays changes in the TP exhaust gas temperature prior to contact with an ORC evaporator located downstream. In addition, the heat exchanger itself has thermal inertia, further dampening the response of the ORC working fluid from changes in engine exhaust gas temperature. These delays vary with material composition and design of both the aftertreatment components and the evaporator itself. An example of evaporator thermal inertia change by varying mass of the tube wall is shown in Fig. 2. As the mass increases, the delay of the working fluid outlet temperature increases and the response time rises significantly. Feru et al. presented the time constants for the exhaust gas, working fluid, and wall in an ORC-WHR heat exchanger modeling study [11].

Aside from the thermal inertia imposed dynamic dampening, the heat exchanger working fluid flow path volume is also critical for control development. Increasing flow path volume extends the time any working fluid molecule remains in the heat exchanger and reduces the responsiveness of the working fluid outlet temperature and mass flowrate changes.

Most existing control strategies generate reference trajectories via steady-state optimization [12], which does not necessarily hold true during transient operation. Moreover, the disturbance rejection capability of the traditional feedback control is limited. Eventually, the exhaustive proportional-integral-derivative (PID) calibration, whose burden is increased by the aforementioned physical delays in the ORC system, may not fulfill the transient control goals. In order to overcome the limitations of the traditional controls, several advanced control strategies have been proposed: (1) linear model predictive control [13], (2) nonlinear model predictive control (NMPC) [14–16], (3) supervisory predictive control [17], dynamic programming [18,19], and (4) extended prediction self-adaptive control [20]. Even though these advanced controls addressed the disadvantages of traditional PID control and showed good results in simulation, they have not been experimentally validated and have raised concerns regarding real-time implementation due to their computational burden. The simulation studies above did not address computation time, and the control designs proposed are still far from experimental implementation.

Only a few experimental ORC-WHR control studies can be found in the literature. Hernandez et al. compared ORC-WHR experimental results for PID and model predictive control (MPC) [21]. In their work, both the PID and MPC utilized the working fluid pump speed as an output to regulate the working fluid temperature at the evaporator outlet. MPC presented a more precise temperature control than PID. This capability ensured low superheat control during transient heat source conditions. Hence, more ORC-WHR power can be produced by MPC than PID, which was also mentioned in Ref. [22]. However, the control-oriented model in Ref. [21] is a first-order lumped model with a time delay transfer function. In order to implement the model over large range of operating conditions, the linear transfer function requires more identification efforts than physics-based models.

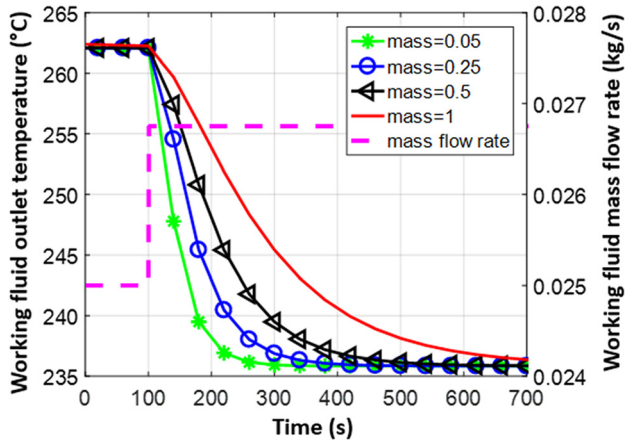

Fig. 2 Working fluid temperature performance at TP heat exchanger outlet during working fluid flow step change. The mass in the legend represents the mass of the tube wall for the shell-and-tubes type heat exchanger and it is normalized by the maximum mass utilized in the simulation.

Peralez et al. presented experimental results for a stand-alone PID and a PID with dynamic inverse model in feedforward control [23]. These controls were implemented on an ORC-WHR system coupled with a HDD engine. The PID with the dynamic inverse model in feedforward showed good working fluid superheat control along multiple engine step changes. However, the working fluid was R245fa, which had a much higher mass flow than high heat capacity working fluids like ethanol or water. ORC working fluid temperature control becomes increasingly challenging as the working fluid mass flowrate decreases. In addition, the evaporation pressure was controlled by a TP exhaust gas bypass valve, which is not an ideal scenario as part of exhaust gas not passing through the heat exchanger. As some of exhaust gas is bypassed, the total amount of heat source is reduced. Thus, the maximum expander power production drops. In the ideal case, all the exhaust gas will pass the evaporator and deliver the maximum amount of heat energy to the working fluid. At the given superheat target, the working fluid mass flowrate will be greater than the exhaust gas partially bypassing case. With the given superheat and greater mass flowrate, the expander can produce more power. In terms of pressure control without exhaust gas bypass, a bypass valve can be added to turbine expander. The turbine bypass valve can easily shift the working fluid mass flow to the turbine without heat transfer delay, which is required by the partially bypassed exhaust gas method. Overall, in the field of ORC-WHR control, many simulation studies are present in the literature but the experimental work is still lacking.

To address this gap in the published knowledge, this paper focuses on experimental validation of a control scheme that includes NMPC for working fluid vapor temperature control in a heavy-duty diesel engine ORC-WHR system. In Ref. [22], the authors proposed and designed a real-time capable augmented control scheme for a HDD engine ORC-WHR system, which ensures efficient and safe operation. Assuming a time constant separation between the thermal and pressure dynamics, a NMPC is designed to regulate the working fluid evaporator outlet temperature, while the evaporator pressure is regulated by an external PID control. The NMPC is designed using a reduced order, moving boundary (MB) control model of the heat exchanger system. In the NMPC formulation, state feedback is constructed from an estimated state (via an extended Kalman filter (EKF)) based on working fluid and exhaust gas temperature measurements at the evaporator outlet. The performance of the control scheme (NMPC plus EKF) is herein experimentally validated via comparison with a conventional, multiloop PID control designed for controlling the evaporator outlet working fluid temperature and the evaporator pressure. In addition, this paper further experimentally validates the proposed augmented control scheme over several sets of transient engine operating conditions and reference working fluid temperatures.

The rest of the paper is organized as follows. Section 2 presents the ORC-WHR system description. Section 3 presents the moving boundary heat exchanger model, which is the six-state control-oriented model in the NMPC. Section 4 presents the NMPC problem formulation and state estimation algorithm. Section 5 discusses the experimental setup, followed by results and analysis in Sec. 6. The paper ends with conclusions in Sec. 7.

2 System Description

An ORC-WHR system coupled to a 13 L HDD engine via a tail-pipe evaporator is considered. The ORC system architecture is shown in Fig. 3. The main components include: (1) a high pressure (HP) pump, (2) a TP evaporator, (3) a turbine expander, and (4) a condenser. Ethanol is utilized as a working fluid in the

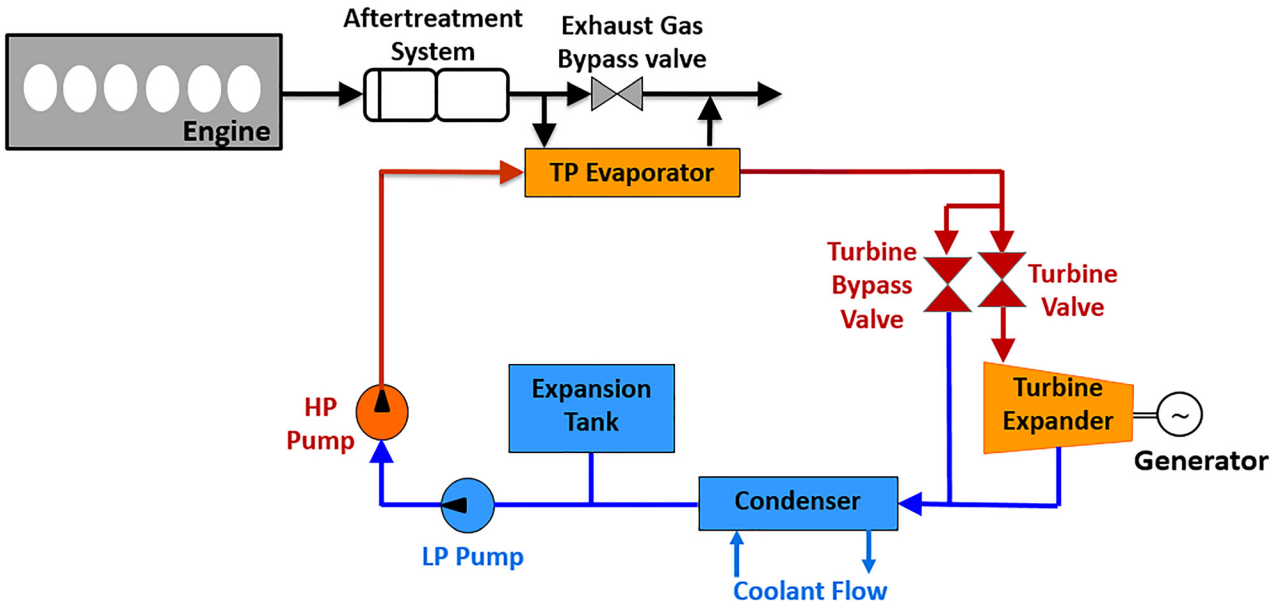

Fig. 3 Schematic of ORC-WHR system

experimental setup. The ethanol is pumped to the TP evaporator by the HP pump, which is an actuation device used to adjust the mass flowrate of ethanol through the evaporator to control the vapor temperature at the evaporator outlet. The evaporator extracts the waste heat from the heat source, subjecting the working fluid to a liquid to vapor phase change. The vapor then passes through the turbine expander and generates electricity. Finally, after passing through the turbine, the ethanol vapor is condensed back to a liquid state in the condenser. Besides the four main components, a reservoir is located downstream of the condenser to supply and absorb working fluid during warmup and transient operating conditions. A low pressure pump is located upstream of HP pump to supply working fluid for HP pump. Two valves are located around the turbine expander to both bypass the working fluid around the turbine during ORC-WHR system warmup and control the evaporation pressure.

3 Evaporator Modeling

To facilitate the control design, a six-state physics-based model is developed for the TP evaporator. In this regard, the heat transfer between working fluid and exhaust gas inside the evaporator is modeled based on conservation of mass and energy balance. The heat exchanger model assumes tube-and-shell construction where the exhaust gas and working fluid flows are separated by wall. As a result, the energy balance is considered in three separate media: the working fluid, the wall, and the exhaust gas. In addition, mass balance is considered for working fluid only to simulate the flowrate as ethanol undergoes the phase change phenomenon. To simplify the heat exchanger model, the following two assumptions are made: (1) the heat conduction in the axial direction of the evaporator is neglected for all media (working fluid, exhaust gas, and wall) and (2) vapor inside heat exchanger is assumed to be incompressible. For an extended discussion and other modeling considerations, one can refer to Refs. [24–26]. The following coupled, one-dimensional partial differential equations along the working fluid flow direction (z-axis) summarize the evaporator model.

Mass balance of working fluid

$$\frac{\partial A_f \rho_f}{\partial t} + \frac{\partial \dot{m}_f}{\partial z} = 0 \tag{1}$$

Energy balance of working fluid

$$\rho_f A_f \frac{\partial h_f}{\partial t} = -\dot{m}_f L \frac{\partial h_f}{\partial z} + \pi d_{t,\text{inner}} U_{f,w}(T_w - T_f) \tag{2}$$

Energy balance of tube wall

$$\rho_w C_{p,w} V_w \frac{\partial T_w}{\partial t} = -A_{f,w} U_{f,w}(T_w - T_f) - A_{g,w} U_{g,w}(T_w - T_g) \tag{3}$$

The heat transfer area between the working fluid and the tube wall is $A_{f,w} = \pi d_{t,\text{inner}} L$; the heat transfer area between the exhaust gas and the tube wall is $A_{g,w} = \pi d_{t,\text{out}} L$.

Energy balance of exhaust gas

$$\rho_g C_{p,g} L \frac{\partial T_g}{\partial t} = \dot{m}_g C_{p,g} L \frac{\partial T_g}{\partial z} + \pi d_{t,\text{out}} U_{g,w}(T_w - T_g) \tag{4}$$

For numerical tractability, the exhaust gas enthalpy is approximated by $h_g = C_{pg} T_g$. The density and specific heat capacity of exhaust gas are considered constant, while working fluid density changes as a function of enthalpy and pressure.

For control design, a three-cell discretization using a MB approach converts the infinite dimensional problem of the coupled partial differential equations in Eq. (1) into a finite dimensional problem of ordinary differential equations. A schematic of the MB model discretization is Fig. 4. The main idea with the MB method is to dynamically track the lengths of the different working fluid phases (liquid, two-phase, and vapor) along the evaporator while applying the same governing differential equations in Eq. (1) to each region using control volumes [27].

Lumped differential equations are derived by integrating the mass and energy conservation equations. The derivation procedure detailed in Ref. [28] is followed to generate a sixth-order ordinary differential equation system. The exhaust gas mass flow dynamics are neglected due to their fast transient characteristics, resulting in a six-state MB model that includes three wall temperatures ($T_{w,1}, T_{w,2}$, and $T_{w,3}$), two phase length (L_1 and L_2), and the working fluid outlet enthalpy ($h_{f,\text{out}}$). The six-state MB model can be derived phase by phase and the details can be found in Ref. [22].

Moving boundary model dynamics are written in standard nonlinear state space form in Eq. (5) for the control formulation purposes

$$\begin{cases} \dot{x} = f(x, z, w, u) \\ 0 = g(x, z, w) \end{cases} \tag{5}$$

where $x = [L_1, L_2, T_{w,1}, T_{w,2}, T_{w,3}, h_{f,\text{out}}]^T$ is a dynamic state vector; $z = [T_{g,1}, T_{g,2}, T_{g,3}]^T$ is an algebraic state vector;

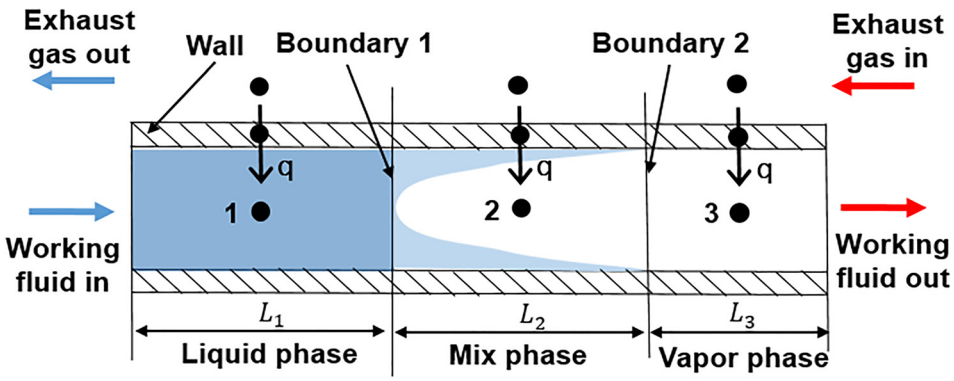

Fig. 4 MB method for evaporator modeling. Exhaust gas and working fluid flow in opposing directions. Heat released from the exhaust gas flows into the working fluid through the thermal mass of the wall.

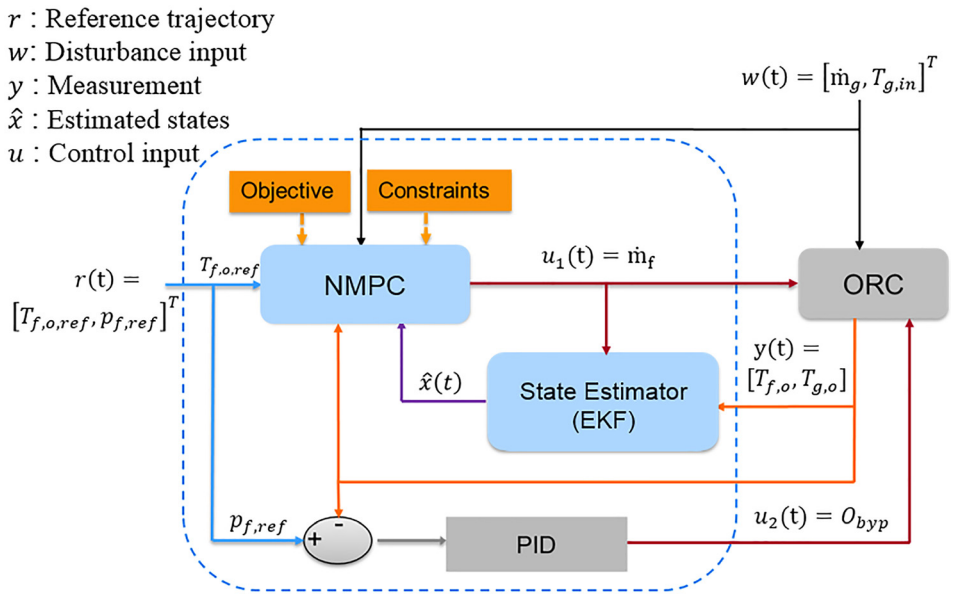

Fig. 5 Augmented control scheme of NMPC plus EKF control

$0 = g(x, z, w)$ represents the algebraic relations; $u = \dot{m}_{f,\text{in}}$ is a control input; and $w = [\dot{m}_g, T_{g,\text{in}}]^T$ is an exogenous disturbance vector (measured disturbance in engine exhaust system).

Pressure dynamics are derived from modeling the compressible working fluid vapor in the pipes between the evaporators, the turbine inlet valve, and the turbine bypass valve. The same conservation principles are applied to this compressible vapor volume. In this study, we limit the ORC-WHR component modeling discussion to the evaporators only. For a description of the remaining component models, as well as experimental model validation, one can consult [26]. The moving boundary model assumes the coexistence of all three phases of working fluid along the evaporator.

4 Control Design

In this section, two closed-loop control algorithms are formulated: (1) an augmented control scheme of NMPC plus EKF, as shown in Fig. 5 and (2) a multiple-loop PID control scheme, as shown in Fig. 6. In the first control scheme, NMPC is used to regulate evaporator outlet temperature, while the evaporator pressure is externally controlled by a PID. In the second control scheme, a traditional multiple-loop PID control with a feedforward term is used for both evaporator outlet temperature and pressure control. In both control schemes, the same control inputs and actuators are used. The control variables are (1) the mass flowrate rate of ethanol ($\dot{m}_f$) for the control of evaporator outlet temperature and (2) the turbine bypass valve opening (O_{byp}) for evaporator pressure control. In the first control scheme, an EKF is used to estimate unmeasured states and provide full state feedback using the measured exhaust gas and working fluid temperatures at the evaporator outlet. The unmeasured states calculated by the EKF are the two working fluid phase lengths (L_1 and L_2) and the three wall temperature states (T_{w1}, T_{w2}, and T_{w3}). The measured disturbances entering the control model are TP exhaust gas mass flowrate and temperature at the evaporator inlet.

4.1 Nonlinear Model Predictive Control Formulation. The NMPC problem formulation is given as follows:

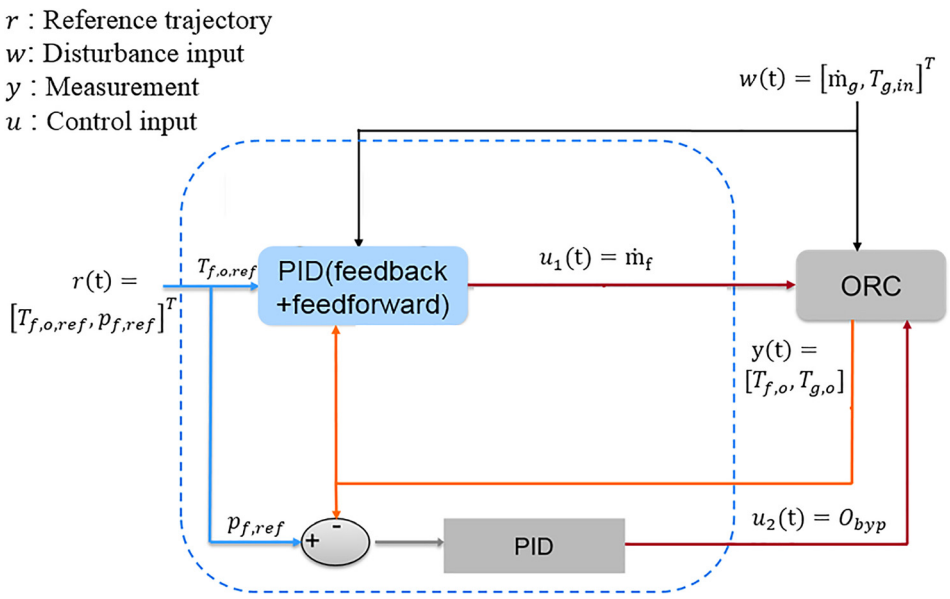

Fig. 6 Multiple-loop PID control scheme

$$\min_{\bar{u}(\cdot),\bar{x}(\cdot)} J(\hat{x}(t_i),\bar{u}(.)) \tag{6}$$

$$\text{s.t}: \begin{cases} \dot{\bar{x}}(\tau) = f\big(\bar{x}(\tau),\bar{z}(\tau),u(\tau),w(t_i)\big),\ \bar{x}(t_i)=\hat{x}(t_i) \\ 0 = g\big(\bar{x}(\tau),\bar{u}(\tau),w(t_i)\big), \\ \bar{y}(\tau) = h\big(\bar{x}(\tau),\bar{z}(\tau),\bar{u}(\tau),w(t_i)\big) \end{cases}$$

$$\begin{aligned} & y^{\text{lb}} \le \bar{y}(\tau) \le y^{\text{ub}}, && \forall\tau\in[t_i,\ t_i+T_p] \\ & u^{\text{lb}} \le \bar{u}(\tau) \le u^{\text{ub}}, && \forall\tau\in[t_i,\ t_i+T_c] \\ & \bar{u}(\tau) = \bar{u}(t_i+T_c), && \forall\tau\in[t_i+T_c,\ t_i+T_{\text{p}}] \\ & x^{\text{lb}} \le \bar{x}(\tau) \le x^{\text{ub}} \end{aligned} \tag{7}$$

$$J = \int_{t_i}^{t_i+T_p} \left\{ B\frac{(T_d - T_{f,o})^2}{T_{f,\max}^2} + (I-B)\frac{du_f^2}{u_{f,\max}^2} \right\} d\tau$$

where $J : \mathbb{R}^{\text{n}} \times \mathbb{R}^{\text{m}} \to \mathbb{R}$ is the cost function; n and m are the state and input dimensions, repectively; the bar $(\bar{\cdot})$ denotes predicted variables based on the control model using the estimated state feedback, $\hat{x}(t_i)$, and predicted input $\bar{u}$; the superscripts lb and ub indicate the lower and upper bounds of the constrained variables, respectively; T_p and T_c denote the prediction and control horizons, respectively with $T_p \ge T_c$; B is the weight of the temperature error term; and $T_{f,\max}$ and $\dot{m}_{f,\max}$ are the maximum working fluid temperature and mass flowrate, respectively. The upper boundary of the working fluid temperature (y^{ub}) is the working fluid decomposition and degradation temperature. The lower boundary (y^{lb}) is the saturation temperature to avoid ingestion of liquid working fluid by the turbine expander, which would be detrimental to the device's health. The input limits (u^{lb} and u^{ub}) are set by the minimum and maximum physical mass flowrates from the HP pump. In addition, the mass flow change rate ($\delta\dot{u}^{\text{lb}}$ and $\delta\dot{u}^{\text{ub}}$) is constrained by the physical capability of the HP pump. The primary goal of the control is working fluid vapor temperature tracking as the temperature tracking error is expressed as $T_d - T_{f,o}$ in Eq. (7). The temperature reference is usually obtained offline by optimizing the turbine power production [29]. In this study, a step change temperature reference and constant temperature reference is used for the demonstration of NMPC temperature tracking performance. The secondary goal is pump speed minimization for the purpose of power consumption saving and this goal is considered in the second term of Eq. (7). The reduction of pump power consumption is beneficial to the system net power production.

The PID feedback and feedforward control are explained in Eq. (8). The feedback portion is shown in the first bracket and outlines the proportional, integral, and derivative terms, respectively. The final term in Eq. (8) is the feedforward part, which is a function of the exhaust gas waste heat power expressed in Eq. (9). In Eq. (9), $\dot{m}_{TP}$, c_p, $T_{TP,\text{in}}$, and T_{amb} represent exhaust gas mass flowrate, specific heat capacity, temperature, and ambient temperature, respectively. The ORC-WHR pressure control utilized the same PID structure as the temperature PID control

$$u(t) = \left[K_p e(t) + K_i \int_0^t e(\tau)d\tau + K_d \frac{de(t)}{dt} \right] + f(P_{\text{waste}}(t)) \tag{8}$$

$$P_{\text{waste}}(t) = \dot{m}_{TP}\Big(t\Big)c_p\Big(t\Big)\big(T_{TP,\text{in}}(t) - T_{\text{amb}}(t)\big) \tag{9}$$

In order to meet real-time implementation constraints with NMPC, the ACADO open source software package is used for efficient real-time code generation [30]. The ACADO tool has previously been employed for dynamic optimization and estimation problems including constrained NMPC [31]. ACADO exports an efficient C++ code based on a direct multiple shooting algorithm. The resulting real-time implementable code exploits the structure of the specific optimization problem by avoiding irrelevant computations.

5 Experimental Setup

A 13 L heavy-duty diesel engine connected to a 440 kW A/C dynamometer in the Clemson University laboratory. The engine control unit is calibrated via ETAS INCA. The ORC system is installed close to the engine and the components are connected according to Fig. 3. The sensor and actuator signal communication are facilitated via controller area network protocol. The entire dyno is monitored by an AVL PUMA data acquisition system. The control schemes are first designed in a MATLAB/SIMULINK environment to generate an executable code, which is later flashed into a dSPACE Micro-Autobox with the following configuration: Gen II 1401/1513, 900 MHz, 16 MB RAM. The schematic of the experimental configuration is shown in Fig. 7.

The engine intake system draws fresh conditioned air from the dyno cell, which is controlled at around 30 °C to ensure the engine

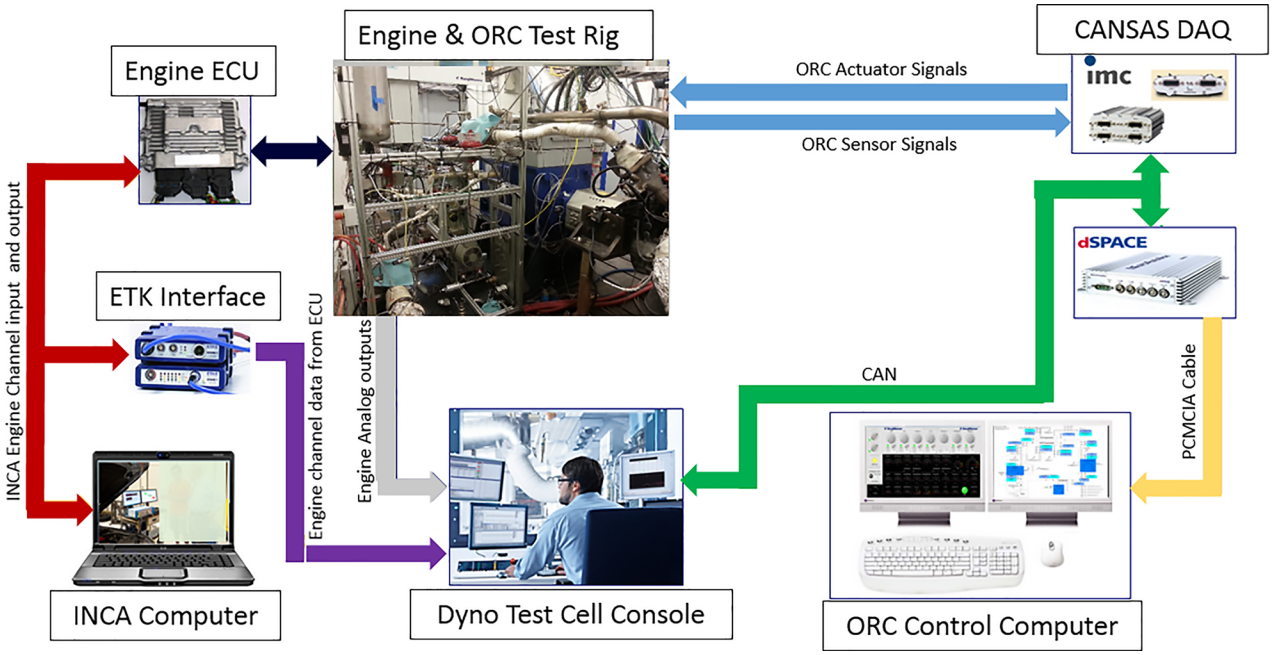

Fig. 7 Experiments configurations for ORC-WHR control testing

intake volumetric efficiency. The engine coolant temperature is held constant through heat exchange with the building cooling water supply. The ORC-WHR condenser is also open-loop cooled by the building cooling water whose temperature at condenser inlet is around 20–25 °C. Turbine power generation is not the focus of this paper. Thus, the turbine is not installed and the turbine inlet valve is held closed during the entire test. The turbine bypass valve is regulated by a PID control to maintain the working fluid evaporation pressure at a nominal point. When turbine is connected to the system, the turbine bypass valve is fully closed and turbine inlet valve is fully open such that all the working fluid passes through the turbine to improve the power generation. In this situation, pressure is left as it is and turbine bypass valve is not activated. There is only one situation that both the turbine bypass valve and turbine are operating. When the turbine inlet pressure is over the system maximum pressure limit, the PID control for the turbine bypass valve is activated to maintain the turbine inlet pressure.

The MB model used for NMPC assumes the existence of three working fluid phases within the evaporator. Thus, in the beginning of each experiment, the EKF estimator engages when working fluid vapor temperature reaches 220 °C, ensuring the presence of all three working fluid phases. When the EKF estimation error reaches a defined threshold, the NMPC is allowed to engage. To ensure stable NMPC engagement, the cost function weight B set to be a small value (e.g., 1×10^{-6}) at the time of engagement, assigning a large cost to the working fluid mass flow change. After the successful NMPC engagement, the cost function weight B is linearly increased to its normal value of 0.99 over a period of 30 s. This sliding weight implementation is a result of offline tuning. Compared to the only weight B tuning in this study, there are multiple parameters to be identified in Ref. [16]: gain, time constant, and time delay, the identification of which are also strict at different steady-state points. However, the NMPC is not extremely sensitive to the weight B variation. That is why the weight B can vary several magnitudes from 1×10^{-6} to 1. The NMPC prediction horizon is set to 60 s and the MB model time-step is 0.6 s.

Turbocharger operation details are not considered in this study as the exhaust gas temperature and mass flowrate directly affect the ORC-WHR system. Different engines have different turbocharger calibration and operation strategies. The exhaust gas temperature and mass flowrate are the results of the turbocharger and engine operations. Exhaust gas mass flowrate and temperature are more direct input comparison than the turbocharger operation strategy comparison. Besides the turbocharger operation, engine fueling, injection timing, exhaust gas recirculation valve, aftertreatment system calibrations, and control strategies also affect the exhaust gas conditions. Therefore, this study does not include the turbocharger operation information and provide exhaust gas mass flow and temperature profiles for all the transient exhaust conditions.

There are three case studies utilized for experimental validation whose operation is described as follows:

Case study 1: Performance evaluation of the NMPC plus EKF. In this case study, the engine operates at a steady-state point 1200 rpm/1000 N·m. The EKF and NMPC are activated in the middle of the experiments. Then, working fluid temperature reference is subjected to multiple step changes.

Case study 2: Performance comparison of two control schemes (NMPC and multiple-loop PID). In this case study, the PID and NMPC performance is compared during an engine step change from 1200 rpm/1000 N·m to 1300 rpm/1200 N·m. The PID and NMPC working fluid temperature controls are implemented in two separate tests, which share the same engine speed and torque profiles.

Case study 3: Performance study of NMPC over transient engine operating points and stepped reference temperature is evaluated during three test cases.

Test 1. The engine operating conditions undergo a step change from 1200 rpm/1000 N·m to 1300 rpm/1200 N·m, while the working fluid vapor temperature undergoes step change from 240 °C to 220 °C and back to 240 °C.

Test 2. The engine operating conditions undergo a step change from 1300 rpm/1200 N·m to 1200 rpm/1000 N·m, while the working fluid vapor temperature reference undergoes a step change from 250 °C to 260 °C.

Test 3. Multiple engine speed/torque step changes are implemented as shown in Fig. 8. Meanwhile, the working fluid vapor temperature is controlled at a constant 240 °C.

6 Results and Discussion

This section overviews the experimental results for the aforementioned test cases. In the results' plots, the working fluid

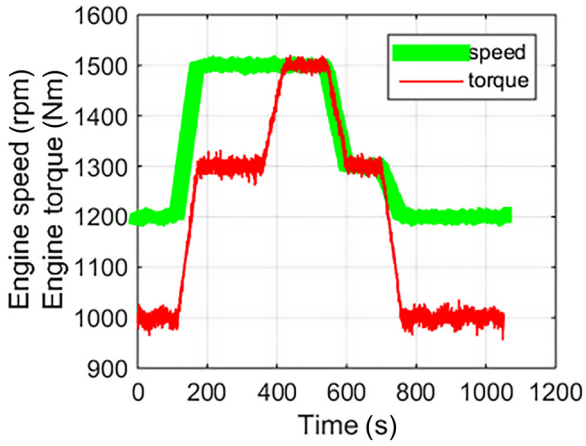

Fig. 8 Transient engine speed/torque

pressure and the working fluid mass flow rate are normalized by corresponding maximum value for in the consideration of sponsor confidentiality.

Case study 1: From Figs. 9(*a*) and 9(*b*), both the estimated working fluid temperature and the estimated exhaust gas temperature exhibit good tracking performance to experimentally measured values. The estimator is activated at the onset of postevaporator vapor detection (∼36 s), as shown in Fig. 9(*a*), and the NMPC is activated once the estimator error falls within the prescribed threshold (∼291 s), as shown in Fig. 9(*d*). In Fig. 9(*c*), working fluid temperature follows the set point closely after NMPC activation at 291 s. Prior to NMPC engagement, the working fluid mass flow rate is controlled by PID controller. This result exhibits successful NMPC plus EKF implementation for heavy-duty diesel ORC-WHR system control during steady-state engine operation.

Case study 2: The PID and NMPC vapor temperature control are compared during an engine step change. The PID gains are extensively tuned in experiments at engine transient conditions and working fluid temperature step change scenarios. Each of the P, I, and D gains are saved in a three-dimensional table given exhaust gas waste heat power and working fluid evaporation pressure as the inputs. The experimental results are shown in Fig. 10. All the data shown in the plots are experimentally measured data. Subplots (*a*) and (*b*) show that the measured engine speed and torque profiles are the same for both the multiple-loop PID and NMPC control scheme tests. Subplots (*c*) and (*d*) show the measured TP exhaust gas temperature and mass flow rate at evaporator inlet, providing further proof that the two experiments are providing nearly identical ORC-WHR inputs to the respective controllers. Subplot (*e*) shows the working fluid inlet temperature, which is subject to condenser functionality. The condenser has adequate cooling to maintain constant the working fluid inlet temperature between the two tests. The condenser is cooled by the test cell building water (20–25 °C), which explains the low temperature of the working fluid inlet temperature (26–28 °C). Subplot (*f*) shows that the evaporation pressure of these two tests is similar. Since the turbine inlet valve is closed during these tests, the evaporation pressure can exceed the nominal point during high speed/load engine operation because the conditions surpass the bypass value orifice area design points. The varying pressure supplies an additional challenge to the NMPC due to the varying evaporation

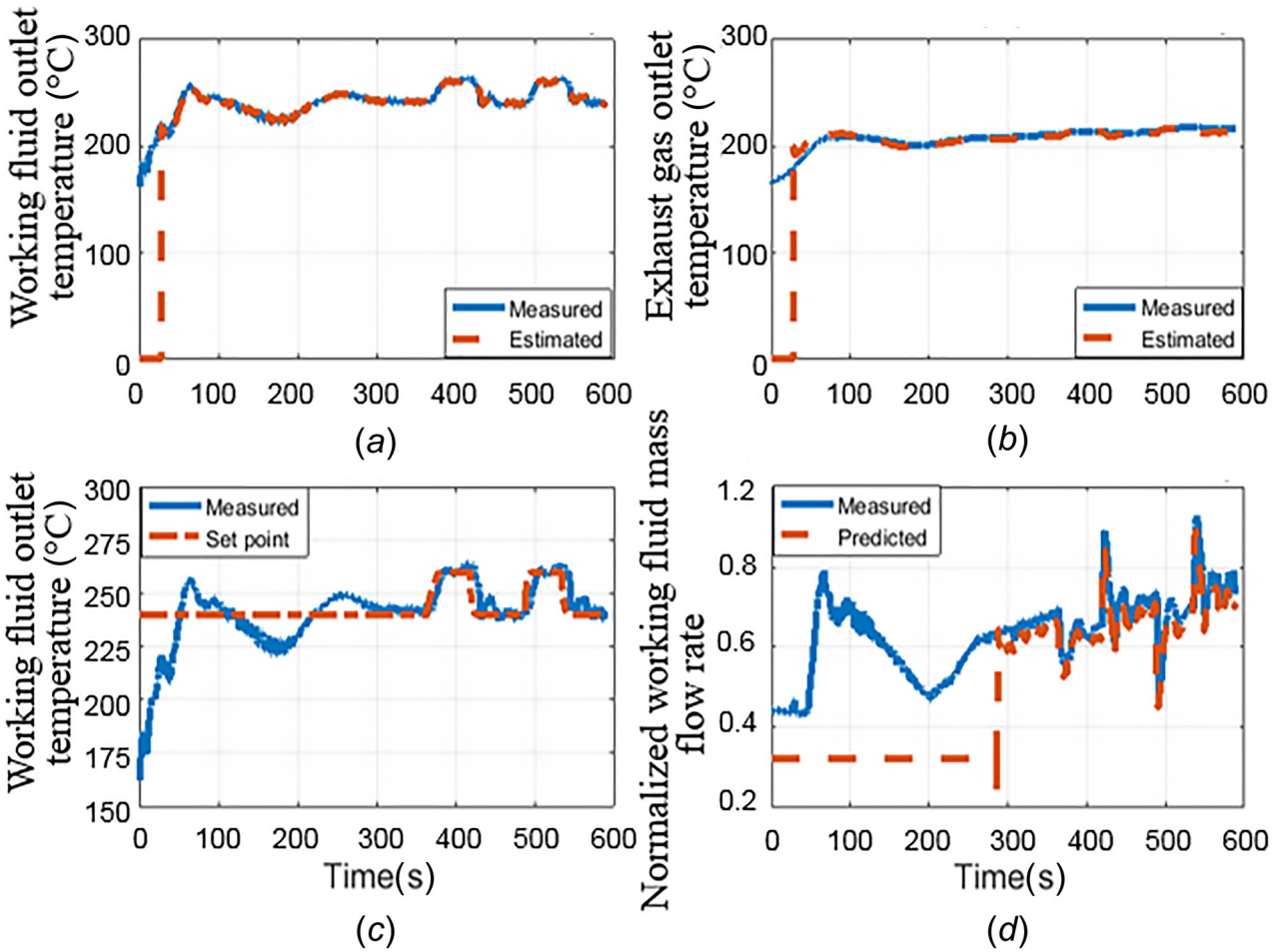

Fig. 9 Case study 1: Performance evaluation of NMPC plus EKF control scheme

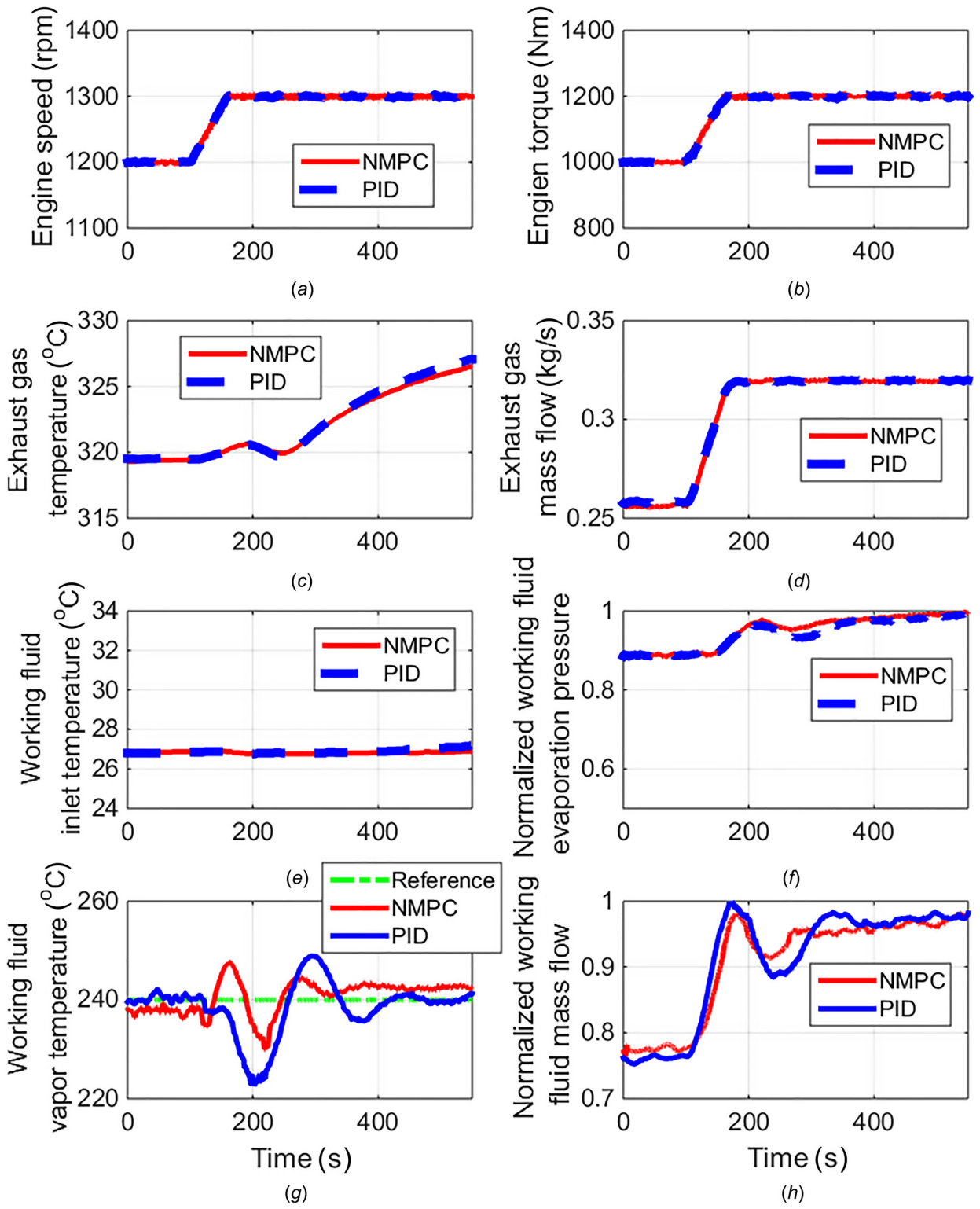

Fig. 10 Case study 2: PID and NMPC comparison at engine step change

temperature. In addition, the varying pressure represents power production conditions when the turbine is running and the bypass valve is closed for the turbine power maximization purpose. During the turbine operation, the pressure ratio is between 10 and 30 and turbine runs in choked flow [26]. In this condition, the evaporation pressure is proportional to the working fluid mass flow rate rather maintaining a constant value. Subplot (*g*) shows the multiple-loop PID and NMPC plus EKF temperature control performance. The NMPC plus EKF reduces the magnitude of temperature oscillations and produces a shorter settling time than the multiple-loop PID control during the engine step change. The temperature performance can be explained by subplot (*h*). Initially (100–200 s), the multiple-loop PID control responds faster than the NMPC because the feedforward in the PID control detects the increase in exhaust mass flow. However, PID working fluid mass flow increases too much, resulting in the large undershoot of working fluid vapor temperature at around 200 s. In comparison, the relatively slower NMPC plus EKF response leads to vapor

temperature increases between 120 and 160 s. Then, the NMPC produces less working fluid mass flow oscillation after 200 s thanks to the future prediction capability. This case study shows an example of NMPC and PID control comparison. More PID and NMPC comparison in the ORC-WHR application can be found in Refs. [13], [20], and [32].

Case study 3 (test 1): The NMPC experimental results from test 1 are shown in Fig. 11. At the constant engine operating condition, the exhaust gas temperature and mass flow rate are almost constant with ± 0.5 °C and ± 0.002 kg/s variation, respectively. In addition, working fluid inlet temperature and evaporation pressure have little variation. At 30 s, the working fluid mass flow starts climbing right after the reference temperature changes. Due to the delay of the heat exchanger, it takes around 10–20 s for the working fluid vapor temperature to drop. The estimated temperature aligns well with the measured temperature. At the first step change, the working fluid mass flow rate increases fast in a very short time to facilitate the working fluid temperature drop. Then, mass flow rate reduces significantly to reduce the temperature undershoot and finally stays stable. Similar phenomenon is observed at the second step change.

Case study 3 (test 2): In this test, both the working fluid vapor temperature reference and the engine speed/torque profile undergo step changes. The NMPC plus EKF experimental results are shown in

Figure 12. Similar to the previous test, the exhaust gas temperature experiences 150 s phase lag due to the aftertreatment system thermal inertia. However, the exhaust mass flow rate decreases simultaneously with engine speed. Working fluid inlet temperature is nearly constant and only increases 0.7 °C during the 520 s test. Working fluid evaporation pressure is also very stable at a nominal reference. The working fluid vapor temperature is well regulated by the NMPC and only minor errors are observed. Working fluid mass flowrate exhibits only small oscillations during the step change.

Case study 3 (test 3): This test is designed to verify the NMPC plus EKF temperature tracking performance over a large range of engine operating conditions. The experimental results are shown in Fig. 13. During the 1050 s test, exhaust gas temperature varies in the range of 288–320 °C and exhaust gas mass flow rate varies from 0.26 kg/s to 0.48 kg/s. The open-loop cooled working fluid inlet temperature varies in narrow range (27–33 °C). During high engine speed and load operating conditions, the turbine bypass valve saturates at its fully open position and working fluid evaporation pressure becomes a function of working fluid mass flow

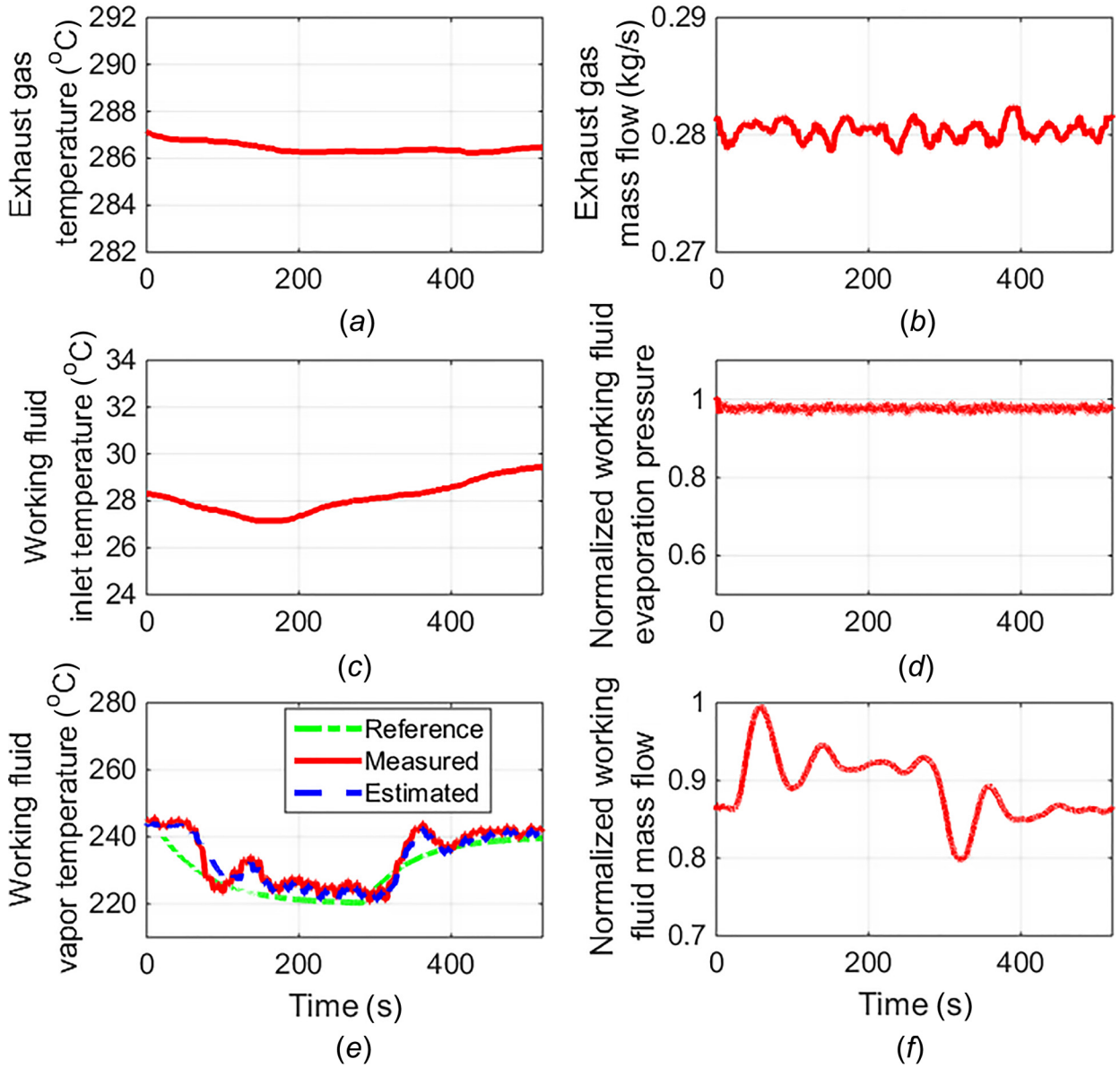

Fig. 11 Case study 3—test 1: constant temperature reference at engine speed/load mild step change

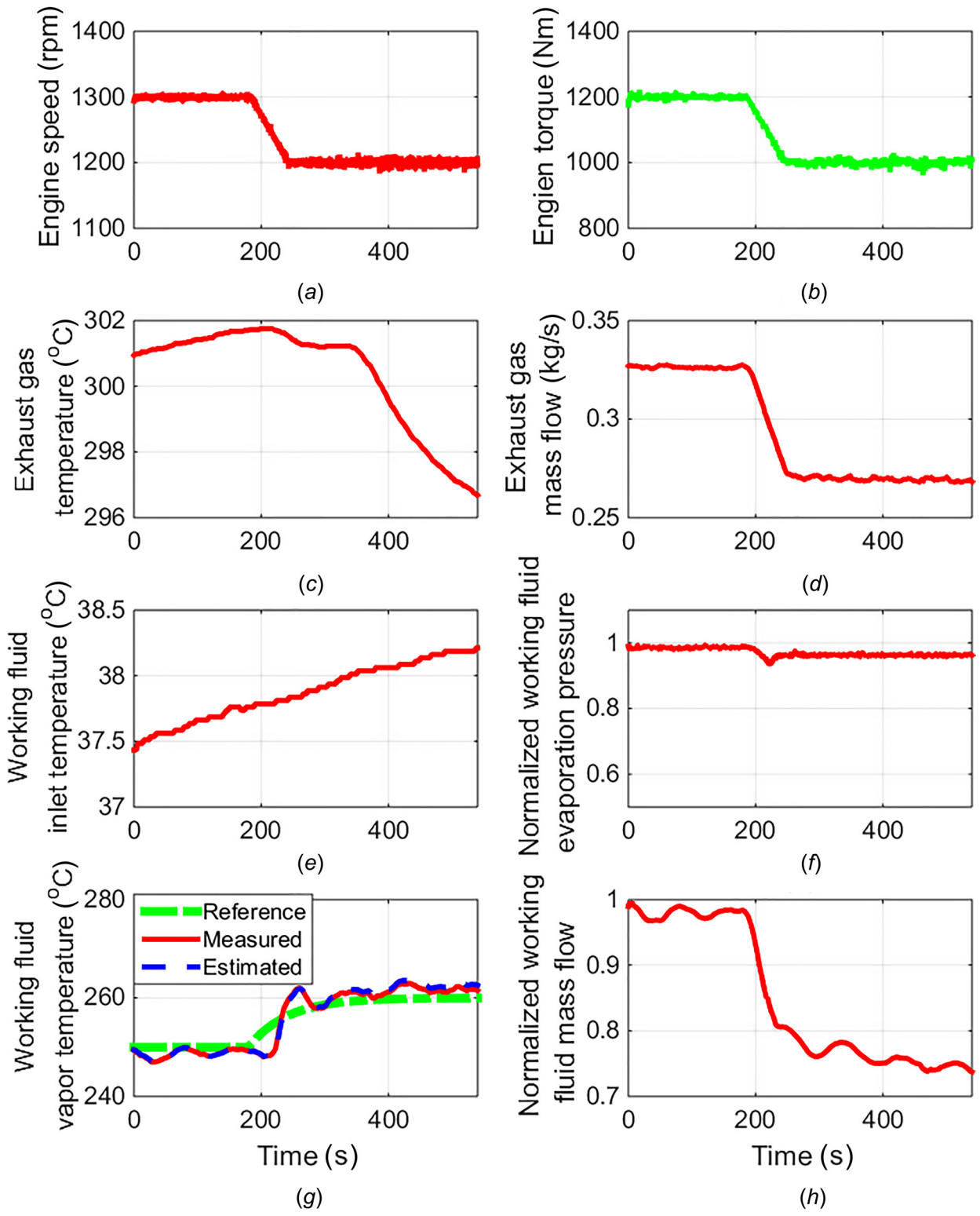

Fig. 12 Case study 3—test 2: temperature step and engine speed/torque mild step

rate. The working fluid vapor temperature experiences its maximum overshoot (15 °C) and undershoot (20 °C) during the first step change. The first step is the most severe step change, inducing a 300 rpm and 300 N·m change to engine operation. The second largest overshoot (13 °C) occurs during the third step change, which is the second most severe. At this step change, engine speed steps down 200 rpm and torque steps down 200 rpm. The constraints of working fluid vapor temperature and working fluid mass flow are also shown in subplots (*g*) and (*h*). It is shown that both constraints are satisfied by NMPC and no constraint violation occurs during the engine speed and torque step changes.

The working fluid vapor temperature mean absolute error, absolute mean error percentage, maximum absolute error, and maximum absolute error percentage from the three tests are shown in Table 1. The temperature error percentage is calculated in degrees Kelvin and the denominator is set as 523 K (i.e., 250 °C). Among

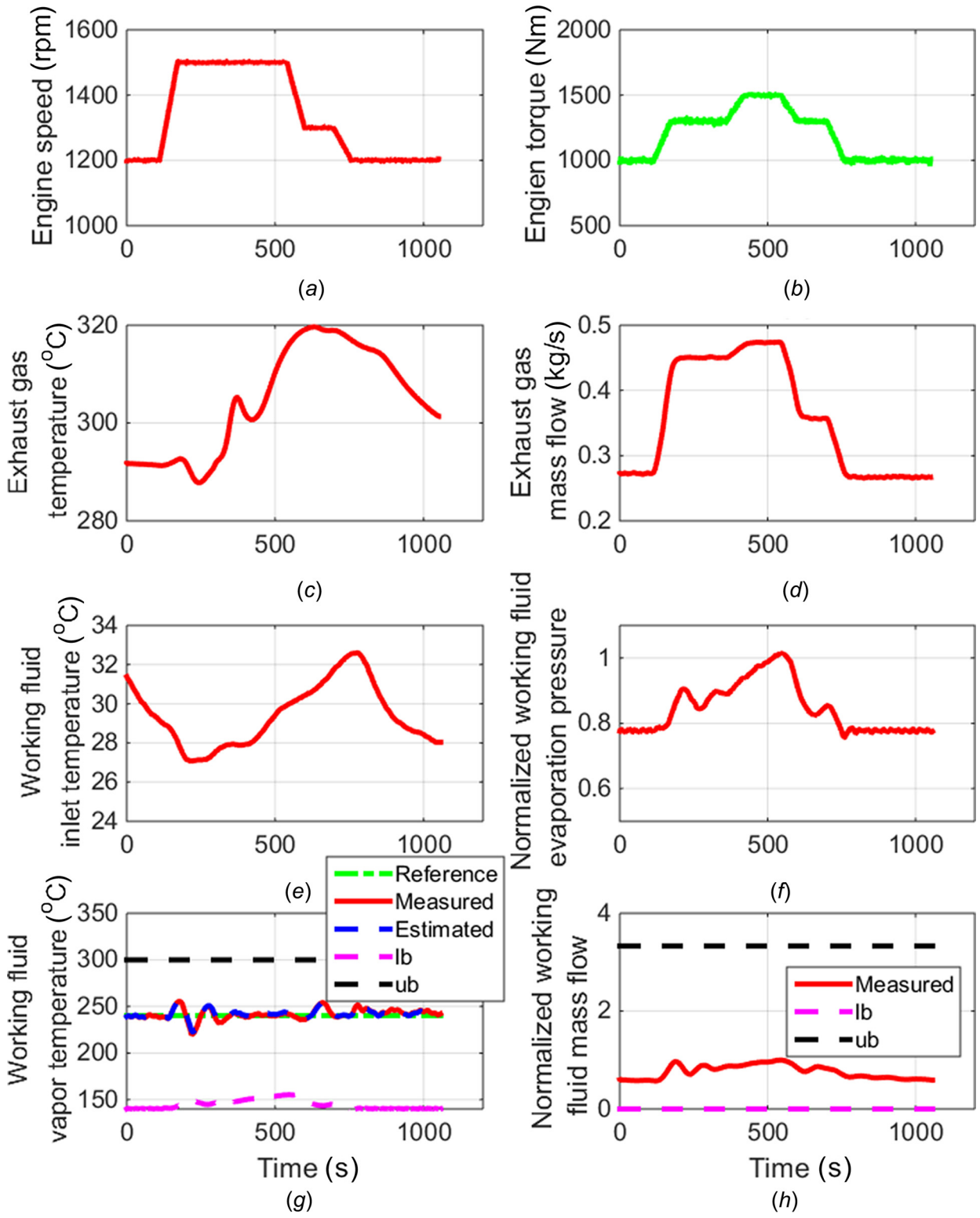

Fig. 13 Case study 3—test 3: constant temperature reference at multiple speed/torque step change

Table 1 Working fluid vapor temperature mean error, mean error percentage, maximum error, and maximum error percentage for the six tests

Case study 3 test number	Working fluid vapor temperature mean absolute error	Working fluid vapor temperature mean absolute error percent	Working fluid vapor temperature maximum absolute error	Working fluid vapor temperature maximum absolute error percent
Test 1	3.4 K	0.65%	10.6 K	2.03%
Test 2	2.1 K	0.39%	5.7 K	1.09%
Test 3	3.9 K	0.75%	20.0 K	3.82%

the three NMPC plus EKF transient tests, the mean absolute working fluid vapor temperature errors are within 5 K or 1%. The maximum absolute temperature error and error percentage are 20 K and 3.82%.

7 Conclusion

In this paper, an augmented working fluid vapor temperature control scheme of NMPC plus EKF is validated in experiments. A complete ORC-WHR system coupled to a 13 L heavy-duty diesel engine is utilized in the experiments. In the transient experiments, the NMPC plus EKF exhibits superior performance relative to a multiple loop PID in terms of error magnitude and settling time. An additional three tests are conducted to verify the NMPC plus EKF capability over different transient scenarios. The results show that the NMPC working fluid vapor temperature tracking mean absolute error is less than 4 K or 1%. The working fluid vapor temperature maximum error percentage can be controlled within 4%.

This control strategy has been validated against multiple engine speed and load step change scenarios. The NMPC plus EKF design can be used for driving cycle working fluid vapor temperature regulation purposes. However, steady-state error caused by the discrepancy between the control-oriented model and the test rig does exist. This could be resolved by adding an integral term within the NMPC. This will be quantified in future work. More importantly, the experimental fuel economy impact will be conducted in the future as it is the final goal of the NMPC. In the fuel economy analysis, the turbine electric and mechanical power production should be compared.

Acknowledgment

This research was conducted as part of a sponsored research contract between Clemson University and BorgWarner, Inc. The authors are thankful for the detailed technical assistance of BorgWarner, Inc.

Nomenclature

A = heat transfer area (m^2)
C_p = heat capacity (J/kg/K)
d = diameter (m)
h = working fluid enthalpy (J/kg)
L = length (m)
$\dot{m}$ = mass flow rate (kg/s)
T = temperature (K)
T = time (s)
U = heat transfer coefficient ($J/m^2/s$)
V = volume (m^3)
z = location in flow axis direction (m)
ρ = density (kg/m^3)

Subscript

f = working fluid
g = exhaust gas
w = wall separating working fluid and exhaust gas
$1, 2, 3$ = liquid phase, mixed phase, and vapor phase

References

[1] Park, T., Teng, H., Hunter, G. L., Velde, B. V. D., and Klaver, J., 2011, "A Rankine Cycle System for Recovering Waste Heat From HD Diesel Engines—Experimental Results," SAE Paper No. 2011-01-1337.
[2] Stanton, D. W., 2013, "Systematic Development of Highly Efficient and Clean Engines to Meet Future Commercial Vehicle Greenhouse Gas Regulations," SAE Int. J. Engines, **6**(3), pp. 1395–1480.
[3] Xu, B., Rathod, D., Yebi, A., Filipi, Z., Onori, S., and Hoffman, M., 2019, "A Comprehensive Review of Organic Rankine Cycle Waste Heat Recovery Systems in Heavy-Duty Diesel Engine Applications," Renewable Sustainable Energy Rev., **107**, pp. 145–170.
[4] Shu, G., Yu, G., Tian, H., Wei, H., Liang, X., and Huang, Z., 2016, "Multi-Approach Evaluations of a Cascade-Organic Rankine Cycle (C-ORC) System Driven by Diesel Engine Waste Heat—Part A: Thermodynamic Evaluations," Energy Convers. Manage., **108**, pp. 579–595.
[5] Teng, H., and Regner, G., 2009, "Improving Fuel Economy for HD Diesel Engines With WHR Rankine Cycle Driven by EGR Cooler Heat Rejection," SAE Paper No. 2009-01-2913.
[6] Teng, H., Regner, G., and Cowland, C., 2007, "Waste Heat Recovery of Heavy-Duty Diesel Engines by Organic Rankine Cycle—Part II: Working Fluids for WHR-ORC," SAE Paper No. 2005-01-0543.
[7] Teng, H., Klaver, J., Park, T., Hunter, G. L., and Velde, B. V. D., 2011, "A Rankine Cycle System for Recovering Waste Heat From HD Diesel Engines—WHR System Development," SAE Paper No. 2011-01-0311.
[8] Nelson, C., 2008, "Exhaust Energy Recovery," DEER Conference, Dearborn, MI, Aug. 4–7.
[9] Nelson, C., 2009, "Exhaust Energy Recovery," Annual Merit Review, Project No. ACE041, Washington, DC, May 18–22.
[10] Nelson, C., 2010, "Exhaust Energy Recovery," Annual Merit Review, Project No. ACE041, Washington, DC, June 7–11.
[11] Feru, E., de Jager, B., Willems, F., and Steinbuch, M., 2014, "Two-Phase Plate-Fin Heat Exchanger Modeling for Waste Heat Recovery Systems in Diesel Engines," Appl. Energy, **133**, pp. 183–196.
[12] Quoilin, S., Aumann, R., Grill, A., Schuster, A., Lemort, V., and Spliethoff, H., 2011, "Dynamic Modeling and Optimal Control Strategy of Waste Heat Recovery Organic Rankine Cycles," Appl. Energy, **88**(6), pp. 2183–2190.
[13] Feru, E., Willems, F., de Jager, B., and Steinbuch, M., 2014, "Model Predictive Control of a Waste Heat Recovery System for Automotive Diesel Engines," Proceedings of the 18th International Conference on System Theory, Sinaia, Romania, Oct. 17–19, pp. 658–663.
[14] Esposito, M. C., Pompini, N., Gambarotta, A., Chandrasekaran, V., Zhou, J., and Canova, M., 2015, "Nonlinear Model Predictive Control of an Organic Rankine Cycle for Exhaust Waste Heat Recovery in Automotive Engines," IFAC-PapersOnLine, **48**(15), pp. 411–418.
[15] Rathod, D., Xu, B., Yebi, A., Vahidi, A., Filipi, Z., and Hoffman, M., 2019, "A Look-Ahead Model Predictive Control Strategy for an Organic Rankine Cycle-Waste Heat Recovery System in a Heavy Duty Diesel Engine Application," SAE Paper No. 0148-7191.
[16] Rathod, D., Xu, B., Filipi, Z., and Hoffman, M., 2019, "An Experimentally Validated, Energy Focused, Optimal Control Strategy for an Organic Rankine Cycle Waste Heat Recovery System," Appl. Energy, **256**, p. 113991.
[17] Hou, G., Sun, R., Hu, G., and Zhang, J., 2011, "Supervisory Predictive Control of Evaporator in Organic Rankine Cycle (ORC) System for Waste Heat Recovery," Advanced Mechatronic Systems (ICAMechS), Zhengzhou, China, Aug. 11–13, pp. 306–311.
[18] Xu, B., Rathod, D., Yebi, A., and Filipi, Z., 2020, "A Comparative Analysis of Real-Time Power Optimization for Organic Rankine Cycle Waste Heat Recovery Systems," Appl. Therm. Eng., **164**, p. 114442.
[19] Xu, B., Yebi, A., Rathod, D., and Filipi, Z., 2019, "Real-Time Realization of Dynamic Programming Using Machine Learning Methods for IC Engine Waste Heat Recovery System Power Optimization," Appl. Energy, **262**, p. 114514.
[20] Hernandez, A., Desideri, A., Ionescu, C., Quoilin, S., Lemort, V., and Keyser, R. D., 2014, "Increasing the Efficiency of Organic Rankine Cycle Technology by Means of Multivariable Predictive Control," IFAC Proc. Vol., **47**(3), pp. 2195–2200.
[21] Hernandez, A., Desideri, A., Gusev, S., Ionescu, C. M., Van Den Broek, M., Quoilin, S., Lemort, V., and De Keyser, R., 2017, "Design and Experimental Validation of an Adaptive Control Law to Maximize the Power Generation of a Small-Scale Waste Heat Recovery System," Appl. Energy, **203**, pp. 549–559.
[22] Yebi, A., Xu, B., Liu, X., Shutty, J., Anschel, P., Filipi, Z., Onori, S., and Hoffman, M., 2017, "Estimation and Predictive Control of a Parallel Evaporator Diesel Engine Waste Heat Recovery System," IEEE Trans. Control Syst. Technol., **27**(1), pp. 282–2954.
[23] Peralez, J., Nadri, M., Dufour, P., Tona, P., and Sciarretta, A., 2017, "Organic Rankine Cycle for Vehicles: Control Design and Experimental Results," IEEE Trans. Control Syst. Technol., **25**(3), pp. 952–965.
[24] Xu, B., Liu, X., Shutty, J., Anschel, P., Onori, S., Filipi, Z., 2016, and M., and Hoffman, "Physics-Based Modeling and Transient Validation of an Organic Rankine Cycle Waste Heat Recovery System for Heavy-Duty Diesel Engine Applications," SAE Paper No. 2016-01-0199.
[25] Xu, B., Rathod, D., Yebi, A., Onori, S., Filipi, Z., and Hoffman, M., 2020, "A Comparative Analysis of Dynamic Evaporator Models for Organic Rankine Cycle Waste Heat Recovery Systems," Appl. Therm. Eng., **165**, p. 114576.
[26] Xu, B., Rathod, D., Kulkarni, S., Yebi, A., Filipi, Z., Onori, S., and Hoffman, M., 2017, "Transient Dynamic Modeling and Validation of an Organic Rankine Cycle Waste Heat Recovery System for Heavy Duty Diesel Engine Applications," Appl. Energy, **205**, pp. 260–279.
[27] Peralez, J., Tona, P., Lepreux, O., Sciarretta, A., Voise, L., Dufour, P., and Nadri, M., 2013, "Improving the Control Performance of an Organic Rankine Cycle System for Waste Heat Recovery From a Heavy-Duty Diesel Engine Using a Model-Based Approach," IEEE 52nd Annual Conference on Decision and Control (CDC), Florence, Italy, Dec. 10–13, pp. 6830–6836.
[28] Jensen, J. M., 2003, "Dynamic Modeling of Thermo-Fluid Systems With Focus on Evaporators for Refrigeration," Ph.D. thesis, Energy Engineering, Department of Mechanical Engineering, Technical University of Denmark, Lyngby, Denmark.

[29] Xu, B., Yebi, A., Onori, S., Filipi, Z., Liu, X., Shutty, J., Anschel, P., and Hoffman, M., 2017, "Transient Power Optimization of an Organic Rankine Cycle Waste Heat Recovery System for Heavy-Duty Diesel Engine Applications," SAE Int. J. Altern. Powertrains, **6**(1), pp. 25–33.
[30] Houska, B., Ferreau, H. J., and Diehl, M., 2011, "ACADO Toolkit—An Open-Source Framework for Automatic Control and Dynamic Optimization," Optimal Control Appl. Methods, **32**(3), pp. 298–312.
[31] Frasch, J. V., Gray, A., Zanon, M., Ferreau, H. J., Sager, S., Borrelli, F., and Diehl, M., 2013, "An Auto-Generated Nonlinear MPC Algorithm for Real-Time Obstacle Avoidance of Ground Vehicles," European Control Conference (ECC), Zurich, Switzerland, July 17–19, pp. 4136–4141.
[32] YebiXu, A., Liu, B., Shutty, X., Anschel, J., Onori, P., Filipi, S. Z., and Hoffman, M., 2016, "Nonlinear Model Predictive Control Strategies for a Parallel Evaporator Diesel Engine Waste Heat Recovery System," ASME Paper No. DSCC2016-9801.